

See discussions, stats, and author profiles for this publication at: <https://www.researchgate.net/publication/232276744>

# Aluminum Plasmonic Nanoantennas

ARTICLE *in* NANO LETTERS · OCTOBER 2012

Impact Factor: 13.59 · DOI: 10.1021/nl303517v · Source: PubMed

---

CITATIONS

135

---

READS

115

9 AUTHORS, INCLUDING:



**Shaunak Mukherjee**

Applied Materials

10 PUBLICATIONS 730 CITATIONS

SEE PROFILE



**Nicholas S King**

Rice University

8 PUBLICATIONS 415 CITATIONS

SEE PROFILE



**Henry O Everitt**

Duke University

190 PUBLICATIONS 2,684 CITATIONS

SEE PROFILE



**Naomi J Halas**

Rice University

328 PUBLICATIONS 34,988 CITATIONS

SEE PROFILE

## Aluminum Plasmonic Nanoantennas

Mark W. Knight,<sup>†,||</sup> Lifei Liu,<sup>‡,||</sup> Yumin Wang,<sup>†,||</sup> Lisa Brown,<sup>§,||</sup> Shaunak Mukherjee,<sup>§,||</sup> Nicholas S. King,<sup>‡,||</sup> Henry O. Everitt,<sup>⊥,¶</sup> Peter Nordlander,<sup>†,‡,||</sup> and Naomi J. Halas<sup>\*,†,‡,§,||</sup>

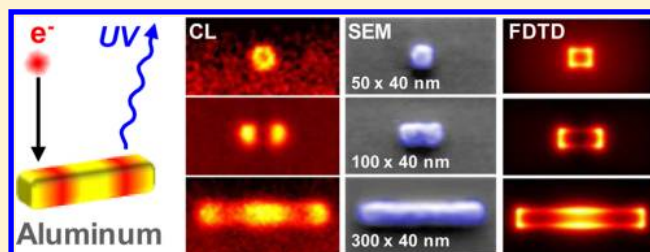
<sup>†</sup>Department of Electrical and Computer Engineering, <sup>‡</sup>Department of Physics and Astronomy, <sup>§</sup>Department of Chemistry, and <sup>||</sup>Laboratory for Nanophotonics, Rice University, Houston, Texas 77005, United States

<sup>⊥</sup>Charles Bowden Research Lab, Army Aviation & Missile RD&E Center, Redstone Arsenal, Alabama 35898, United States

<sup>¶</sup>Department of Physics, Duke University, Durham, North Carolina 27708, United States

**ABSTRACT:** The use of aluminum for plasmonic nanostructures opens up new possibilities, such as access to short-wavelength regions of the spectrum, complementary metal–oxide–semiconductor (CMOS) compatibility, and the possibility of low-cost, sustainable, mass-producible plasmonic materials. Here we examine the properties of individual Al nanorod antennas with cathodoluminescence (CL). This approach allows us to image the local density of optical states (LDOS) of Al nanorod antennas with a spatial resolution less than 20 nm and to identify the radiative modes of these nanostructures across the visible and into the UV spectral range. The results, which agree well with finite difference time domain (FDTD) simulations, lay the groundwork for precise Al plasmonic nanostructure design for a variety of applications.

**KEYWORDS:** Plasmon, UV, cathodoluminescence, nanoparticle, nanorod, aluminum



Plasmonics is currently a field of nanoscience enjoying remarkably rapid growth, due to interest in both its scientific underpinnings as well as its highly promising potential for real-world applications.<sup>1–3</sup> By far, research in this field has utilized the coinage metals—gold, copper, and silver—yet many potential commercial applications would be optimally realized by inexpensive plasmonic materials compatible with either high-tech or high-throughput manufacturing methods. Aluminum is the third most abundant element in the earth's crust, behind oxygen and silicon.<sup>4</sup> It has tremendous potential as a plasmonic material that could potentially serve as the metal of choice for either complementary metal–oxide–semiconductor (CMOS)-compatible or mass-producible plasmonic applications. Unlike the noble metals, the d-band of Al lies above its Fermi energy, allowing for plasmon resonances that extend beyond the visible region of the spectrum into the ultraviolet. The surface oxide of Al self-terminates at a thickness of 2–3 nm, forming a durable protective layer and preserving the metal.<sup>5</sup> Aluminum can exhibit strongly enhanced local fields due to the low screening of Al ( $\epsilon_\infty \approx 1$ ) relative to Au ( $\epsilon_\infty \approx 9$ ) and Ag ( $\epsilon_\infty \approx 4$ ), and to its higher electron density, contributing 3 electrons per atom compared to 1 electron per atom for Au and Ag. Localized plasmon resonances in Al have been demonstrated in several geometries, including spheres,<sup>6–8</sup> triangles,<sup>9,10</sup> discs,<sup>5,11,12</sup> and rods.<sup>13,14</sup> Applications where Al plasmonic nanostructures would be optimal include CMOS-compatible, on-chip plasmonic nanoantennas, waveguides and interconnects, nonlinear plasmonics,<sup>14</sup> inexpensive, disposable SERS substrates,<sup>11,15</sup> enhanced UV fluorescence,<sup>16</sup> and energy harvesting structures.<sup>17</sup>

An emerging tool for the study of plasmonic nanostructures is cathodoluminescence (CL). An energetic electron beam incident on the structure excites many plasmon modes: photon emission from the radiative modes of the structure is then detected. The high degree of spatially localized excitation due to the electron beam focus enables imaging of individual plasmon modes with nanometer-scale spatial resolution.<sup>18</sup> Although CL detects only the radiative modes, it does so without perturbing the local dielectric environment like probe-based imaging and is therefore an ideal experimental method for studying the optical properties of ultrasmall structures. CL images of the plasmonic emission of an individual nanostructure map its wavelength-dependent local density of optical states (LDOS), a measure of the electromagnetic modes into which an electric (or magnetic) dipole may emit.<sup>19,20</sup> The ability to experimentally visualize the LDOS at the single nanoparticle or nanostructure level is leading to the rapid adoption of this method as a powerful characterization tool within the field of nanoscale plasmonics.<sup>21–24</sup>

In this Letter we study the plasmonic properties of individual Al nanorod antennas using CL. We present spatially resolved images of the radiating plasmon modes (LDOS) of Al nanorods with length-tunable resonances from the visible to the UV region of the spectrum. The high degree of spatial and energetic resolution obtained permits direct comparison between numerical simulations and experiment, a crucial first step in

**Received:** September 20, 2012

**Revised:** October 10, 2012

**Published:** October 16, 2012

the development of accurate design tools for many currently envisioned Al plasmonics applications.

The aluminum nanoantennas used in this study were fabricated by planar lithography on lightly doped ( $1\text{--}10\ \Omega\cdot\text{cm}$ ) *n*-type silicon with 30 nm of thermal oxide. This oxide thickness was chosen to isolate the plasmonic response of the resonators from the silicon substrate while minimizing the CL background due to the luminescence of the silica.<sup>25</sup> The nanostructures were patterned with electron beam lithography using  $\sim 70$  nm thick PMMA resist (poly(methyl methacrylate), 950 wt). The aluminum was then deposited either by thermal or electron beam evaporation of pure aluminum, with the rate ( $1.5\ \text{\AA}/\text{s}$ ) and thickness (30 nm) determined in situ with a quartz crystal microbalance (QCM). Due to good adhesion between silica and aluminum, no additional adhesion layer was required, avoiding the plasmonic damping that results from Ti or Cr adhesion layers normally used in the patterning of coinage metal nanostructures.<sup>26</sup> Upon removal from the deposition chamber, a stable, 2–3 nm surface oxide ( $\text{Al}_2\text{O}_3$ ) formed on the nanostructures,<sup>5</sup> encapsulating the remaining aluminum and protecting the devices against environmental degradation. Excess material was removed via liftoff in NMP (1-methyl-2-pyrrolidone) heated to  $60\ ^\circ\text{C}$ , and the sample was rinsed with isopropanol and dried with  $\text{N}_2$ . Scanning electron microscopy (SEM) micrographs of the fabricated structures confirmed that the in-plane experimental dimensions agreed with the nominal dimensions to within measurement error ( $\pm 2$  nm). The 30 nm nanorod thickness, estimated during Al deposition, was confirmed by high angle SEM imaging.

In the CL experiments, a focused electron beam (30 keV) incident on the nanostructure excites the plasmon modes of the structure. The photons emitted from radiative decay of the plasmons are collected by a 0.89 N.A. parabolic mirror and directed into a filter/detector system (Gatan, MonoCL4 Elite) for counting. Raster-scanning the electron beam over the structure while collecting the emitted photons as a function of beam position enables the construction of excitability images proportional to the radiative LDOS of the structure.<sup>19</sup> All CL maps were collected using an electron beam step size of 1.5 nm, yielding images with sufficient spatial oversampling to allow postacquisition noise reduction using a Gaussian low-pass filter. To ensure a sufficiently high photon count rate, all measurements were performed with a  $\sim 2$  nA beam current. Sample contamination during the scans was minimized by performing in situ  $\text{N}_2$  plasma cleaning of the sample and vacuum chamber prior to measurement. All measurements were performed at a chamber pressure of  $\sim 2 \times 10^{-6}$  Torr. Energy selectivity during imaging was achieved by using a combination of bandpass filters and an integrated Czerny–Turner monochromator. The filters selected photons within energy bands from 2.1 to 2.4 eV ( $550 \pm 40$  nm), 2.5 to 3.0 eV ( $450 \pm 40$  nm), and 2.9 to 3.3 eV ( $400 \pm 50$  nm), with the highest energy measurements, spanning 3.3–3.8 eV, taken using the monochromator (150 g/mm). These measurement bandwidths were selected as a compromise between spectral resolution and a photon count rate sufficient for imaging purposes.

Modeling of the structures was performed using the finite difference time domain method (FDTD, Lumerical). The nanorod dimensions were matched to the nominal dimensions specified during lithography, with a 5 nm radius of curvature on all exposed edges. To account for substrate effects, the simulated nanorods were positioned on top of an infinite silica slab. Spectral responses were calculated using normal incidence

plane wave excitation and tabulated dielectric functions for both aluminum and silica.<sup>27</sup> While the CL maps, strictly speaking, should be evaluated as the integrated radiation emitted by locally excited plasmon modes (LDOS),<sup>24</sup> this would be a computationally expensive task. Our CL maps were therefore instead computed using a single plane wave incident on the nanorod at  $75^\circ$  off normal, which allowed excitation of both symmetric and antisymmetric modes. The resulting near-field map, calculated 5 nm above the nanorod surface, should closely approximate the radiative LDOS due to the close relationship between radiative decay probabilities and optical scattering cross sections.

Images of the LDOS were obtained using CL for both the longitudinal and the transverse plasmon modes of a typical Al nanorod antenna (Figure 1). It is well-established that plasmonic nanorods exhibit nondegenerate longitudinal and

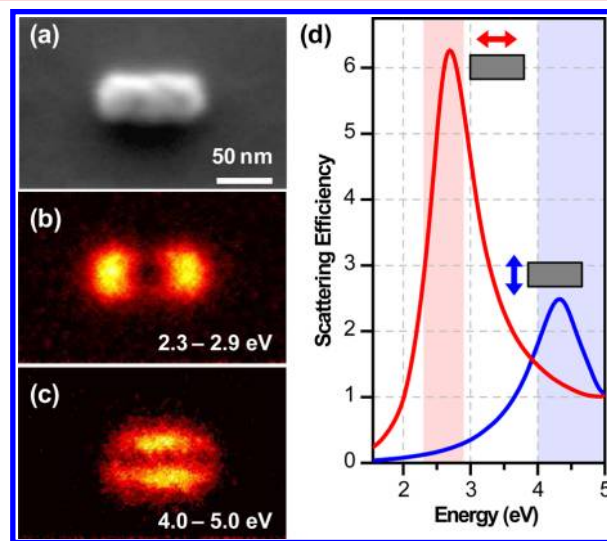


**Figure 1.** Mode-resolved CL images. (a) SEM image of a  $100\text{ nm} \times 40\text{ nm}$  aluminum nanorod and energy-filtered CL images at the (b) longitudinal and (c) transverse plasmon emission peaks. Color scales are normalized. (d) Calculated scattering spectra corresponding to the experimental geometry illustrating the longitudinal (red) and transverse (blue) plasmonic modes. The experimental CL transmission filters used for photon collection for the transverse (b) and longitudinal mode (c) are indicated in (d) as the red and blue shaded regions, respectively.

transverse plasmonic resonances.<sup>28,29</sup> In Al, the nanorod plasmon modes extend from the visible into the UV region of the spectrum. For a  $100\text{ nm} \times 40\text{ nm}$  Al nanorod (Figure 1a), the CL image reveals a longitudinal dipolar resonance when emission between 2.3 and 2.9 eV is collected upon raster-scanning the incident electron beam. For this mode, we clearly observe the highest LDOS at the short nanorod ends (Figure 1b). The transverse plasmon mode, obtained from the collected photon emission in the 4.0–5.0 eV range, shows the LDOS concentrated along the longer nanorod edges (Figure 1c). The photon energy collection ranges used in each of these two images encompass both dipolar modes calculated for the structure (Figure 1d).

From the experimentally obtained maps of the Al nanorod LDOS we can determine the spatial resolution of the present CL imaging. For the transverse mode, which exhibits the highest spatial confinement, we find a spatial full width at half maximum (fwhm) of 20 nm in the measured CL emission. This



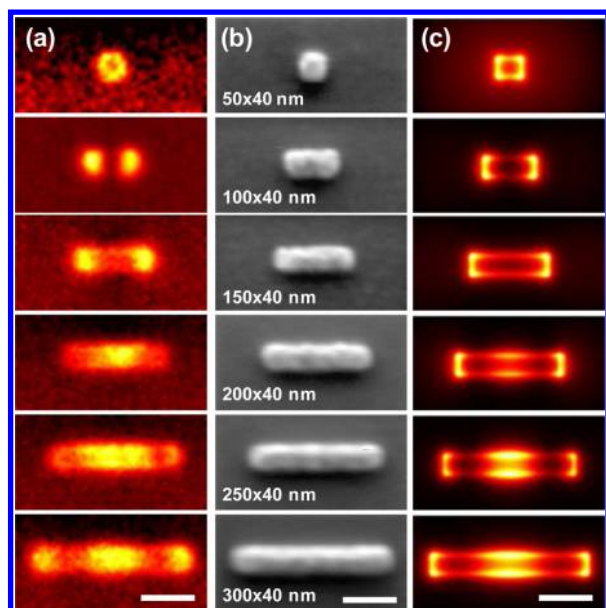


**Figure 2.** Influence of aspect ratio on the CL of single aluminum nanorods. (a) CL excitability images for the energy range 2.5–3.0 eV along with the associated (b) secondary electron images of the nanorods acquired in parallel with CL. (c) Calculated electromagnetic field distributions for the experimental geometry. All scale bars are 100 nm.

is not a direct measure of the resolution, since the mode itself has an associated width, but the fwhm places an upper limit of 20 nm on our achievable spatial resolution. The actual resolution is likely better than 20 nm and is determined primarily by the spot size of the electron beam ( $<5$  nm) and the spatial extent of the evanescent field of the energetic incident electrons,  $\sim v/2\omega$ , where  $v$  is the electron velocity and  $\omega$  is the frequency of the emitted photons.<sup>19</sup> For the spectral window accessed in this study (2.3–5.0 eV), the evanescent field extends from  $\sim 7.5$  nm to  $\sim 15$  nm beyond the electron beam waist and is therefore the primary factor determining the spatial resolution of our CL images.

By measuring the radiative LDOS for several Al nanorod antennas of varying aspect ratios in a fixed spectral window, we may directly observe the geometric dependence of their plasmon modes (Figure 2). For a nearly symmetric, 40 nm  $\times$  50 nm nanoantenna, the longitudinal and transverse modes are essentially degenerate, giving rise to a ring-like radiative LDOS image (Figure 2, top row) in the photon energy detection window between 2.5 and 3 eV. Extending the nanorod to 100 nm length breaks this degeneracy and creates a strong longitudinal dipole mode whose radiation dominates over the transverse mode. As the antenna length is increased further, the longitudinal dipolar resonance shifts to lower photon energies outside the photon energy detection band. As the rod becomes longer, all longitudinal modes redshift. For the longest antenna structure, a longitudinal quadrupolar mode has shifted into the photon energy collection window (Figure 2, bottom row). This strongly radiating linear quadrupolar mode, which would be a nonradiative “dark” mode in the quasistatic limit, is here visible due to phase retardation. Retardation effects are particularly strong for plasmonic Al structures due to their high plasmon energies compared to other metals. The onset of phase retardation and strong radiative coupling occurs when the spatial extent of the structure is larger than nominally a quarter

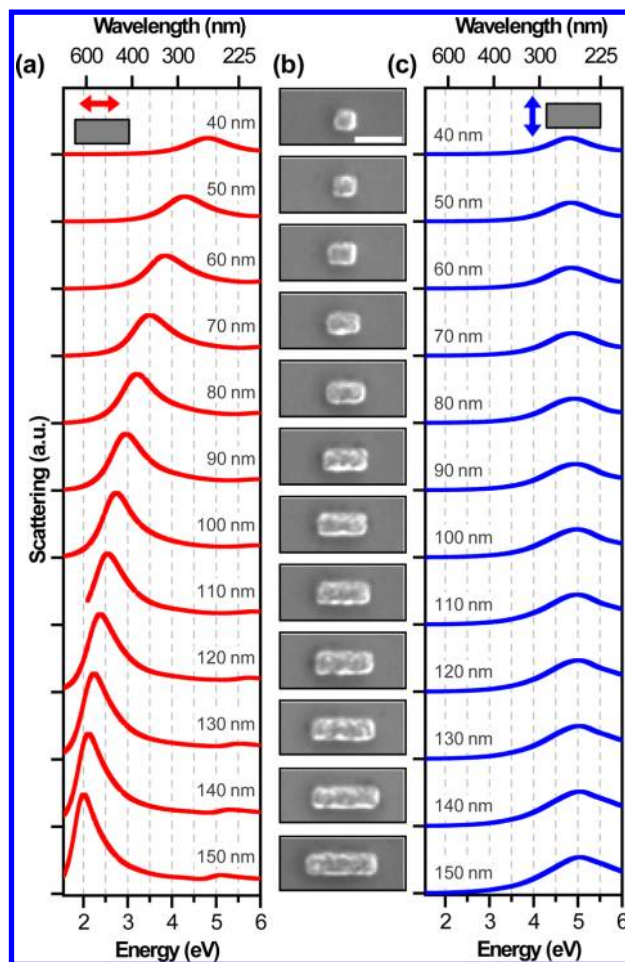


**Figure 3.** Scattering spectra calculated for normal incidence excitation of Al nanorod antennas of increasing length for (a) longitudinal and (c) transverse polarization. The dimensions of the structures are the nominal dimensions of (b) the fabricated Al nanorod antennas. The scale bar is 100 nm.

of the wavelength of the plasmon resonance. The lengths of the nanorod structures in the two bottom panels of Figure 2, 250 and 300 nm, are larger than half the wavelength of their plasmon resonances (300–500 nm) and can very efficiently couple to free space radiation. Clearly one would anticipate additional higher order radiative modes if the absolute length of the nanoantenna was further increased.

The agreement between the experimentally measured CL maps and the calculated LDOS is excellent. The small differences between the LDOS amplitudes at the rod ends relative to the center may be the result of the  $\text{Al}_2\text{O}_3$  capping layer or the presence of grain boundaries in the Al nanostructures, both of which could modify the resonance frequency and charge distribution of the nanostructure. In our simulations a pure aluminum structure with a local dielectric function corresponding to bulk Al was assumed;<sup>27</sup> nonlocal effects and possible deviations from bulk dielectric values were not included. Another contribution to the slight discrepancy could be due to our simple approximation of the radiative LDOS as the total field enhancement 5 nm above the particle under plane wave excitation. In CL, the incident electron beam can be viewed as a line current density source which can interact only with the vertical field component of the plasmonic mode.<sup>24</sup>

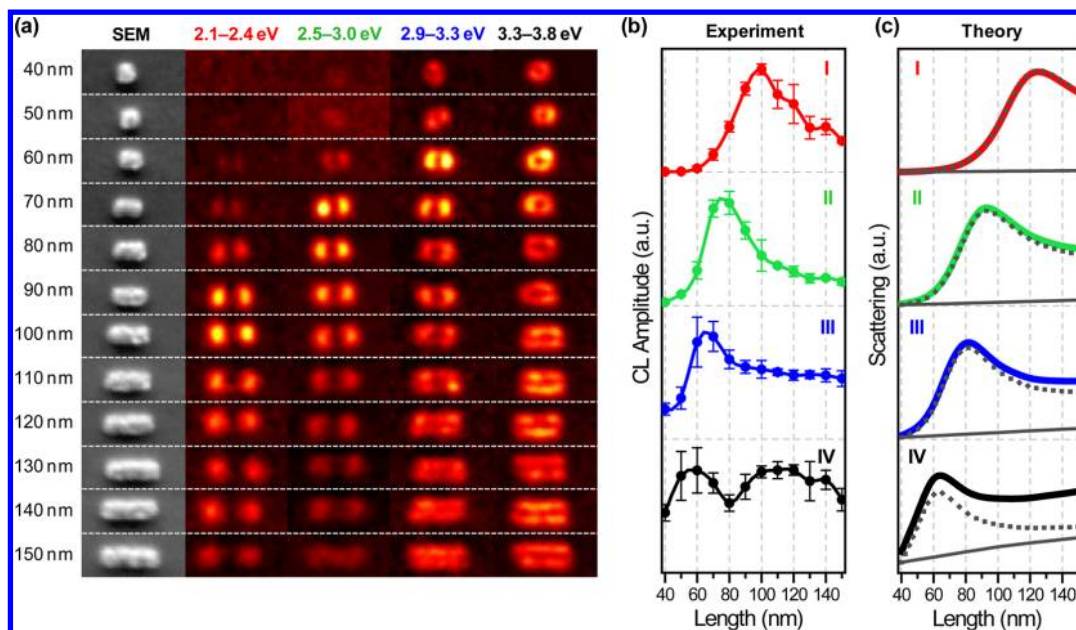


**Figure 4.** (a) SEM images with the associated CL images of individual aluminum nanorod antennas obtained for antenna lengths varied from 40 to 150 nm (horizontal rows), over a range of four photon energy collection windows: 2.1–2.4 eV, 2.5–3.0 eV, 2.9–3.3 eV, and 3.3–3.8 eV (vertical columns). The color scale of the images is normalized for each photon energy collection window. (b) Normalized CL emission intensity for each wire length at 2.1–2.4 eV (I, red), 2.5–3.0 eV (II, green), 2.9–3.3 eV (III, blue), and 3.3–3.8 eV (IV, black). (c) Calculated scattering amplitudes for excitation at 2.4 eV (I, red), 3.0 eV (II, green), 3.3 eV (III, blue), and 3.8 eV (IV, black) as a function of antenna length. The relative longitudinal and transverse contributions are indicated by dotted and solid gray lines, respectively.

Background noise in the experimental CL images is due to a combination of luminescence from the substrate and transition radiation (TR), which results when an energetic electron crosses the interface between two disparate dielectric media.<sup>18,25</sup> The substrate luminescence likely originates from point defects in the silica layer.<sup>25</sup> However, within the 2.5–3.0 eV photon collection range, emission from radiative plasmon modes clearly dominates the images, allowing us to easily resolve the plasmon modes against a relatively weak background signal.

In Figure 3, we show the calculated scattering spectra for a series of Al nanorods of increasing length that also will be used in CL imaging. As the nanorod antenna becomes longer, the longitudinal dipole resonance shifts to lower energies and narrows, and higher order longitudinal modes begin to emerge (Figure 3a). In contrast, the transverse resonance is only very weakly dependent on nanorod length, exhibiting a slight blue shift with increasing rod length (Figure 3c). Both longitudinal and transverse modes exhibit increased scattering with rod length. Since our calculations were performed using normal incidence plane wave excitation, these spectra show only the odd numbered “bright” modes ( $n = 1, n = 3, \dots$ ) with finite dipole moments. Also, while the peak width decreases monotonically across our simulated spectral range as the peak shifts to lower energies, there should be a subsequent increase in the fwhm near 1.5 eV due to interband transitions.<sup>5</sup>

In Figure 4 we use energy-resolved CL imaging to visualize the spatial dependence of the LDOS across four different energy windows in the 2–4 eV photon energy range for the structures shown in Figure 3. For the smallest nanorod antennas with degenerate longitudinal and transverse modes (40 nm  $\times$  40 nm nanorods) we observe a ring-shaped excitability map across the entire spectral range, with the greatest emission intensity at the highest photon energies (Figure 4a). For longer nanorod antennas, distinct transverse

and longitudinal resonances are again observed. For a given energy window, as the nanorod length is increased, the longitudinal mode first strengthens and then weakens, as the resonance redshifts across the collection window. For the lowest photon energy collection window (2.1–2.4 eV, first column), only dipolar emission from the longitudinal mode is observed. For the three higher photon energy collection ranges, a significant evolution in the LDOS image is observed, transitioning from longitudinal to transverse radiators as the antenna length increases. The emission intensity for each energy range is maximized by a nanorod antenna of a particular length.

These experimental trends can be compared with the simulations presented in Figure 3 by extracting the relative scattering amplitude from each nanorod antenna from the normalized LDOS images. In this analysis (Figure 4b), the background emission is removed from the measured integrated emission intensity. For each antenna length and photon energy collection window, the integrated emission intensity was obtained from CL images of four individual nanoantennas. The error bars on each experimental data point show the standard deviation due to antenna-to-antenna size variation for four nominally identical nanorods.

The experimental scattering response exhibits a distinct antenna length dependence within each photon energy collection window (Figure 4b). For the lowest photon energy range (Figure 4b, I), a single distinct maximum is observed, corresponding to a 100  $\times$  40 nm nanorod antenna whose dipolar plasmon directly overlaps this photon energy range. The radiative decay from the nanorod plasmons tuned to either side of this collection window cannot be captured as efficiently. The asymmetry of the emission peak results from the weaker scattering intensity of the shorter nanorods. This single, asymmetric peak is reproduced well in the FDTD calculations,



where the dipolar scattering cross sections as a function of rod length are plotted (Figure 4c, I).

In the higher photon energy collection windows, the emission peak shifts toward shorter nanorods, but with a relative increase in the emission observed for longer nanorod antennas (Figure 4b–c, II–IV). The shift in the emission peak from 100 to 60 nm nanorod length is attributable to the blueshift of the nanorod resonance with decreasing length (seen also in Figure 3b). The increased emission for longer rods is due both to the increased radiation from longer rods and to a change in the relative emission amplitudes of the transverse and longitudinal resonances (Figure 4c). When the theoretical emission intensity is decomposed into its relative longitudinal and transverse contributions (dotted and solid lines, respectively), we see that the transverse contribution is negligible for low energy resonances (I). At higher energies the transverse contribution increases (II, III), and for the highest photon energy range measured (3.3–3.8 eV), the transverse mode emits photons as efficiently as the longitudinal mode (IV). The agreement between the measured and the calculated emission intensities is excellent for the three lowest photon energy windows. For the highest photon collection window (Figure 4b,c, IV), the measured emission exhibits a clear peak at 60 nm corresponding to the longitudinal resonance and a second rise in emission for longer nanorods. This broad peak, which can be clearly visualized as the transverse resonance (Figure 4a), only appears in the calculated response as a rise in intensity. This discrepancy may be due to measurement error, given that the 3.3–3.8 eV bandpass yielded the lowest photon count rate. It is also possible that surface effects, such as the presence of the thin Al<sub>2</sub>O<sub>3</sub> oxide layer or grain structure, may play a role; surface effects can exert significantly more influence on the electromagnetic response at higher energies.

In conclusion, we have examined the plasmonic properties of Al nanorod antennas, which exhibit highly tunable plasmonic resonances from the deep UV through the visible region of the spectrum. The radiative nanoantenna resonances, which include dipolar and quadrupolar plasmon modes, were imaged using energy-resolved CL, with a spatial resolution of nominally 20 nm. The dependence of the nanoantenna radiative modes on antenna length and photon energy was found to agree well with FDTD-based analysis of these nanostructures. Our results suggest that aluminum provides a practical and highly promising material system for the design and implementation of UV and visible frequency plasmonics, broadening the range of potential applications of plasmonics into areas where CMOS compatibility or low-cost, mass producibility are desired.

## AUTHOR INFORMATION

### Corresponding Author

\*E-mail: halas@rice.edu.

### Notes

The authors declare no competing financial interest.

## ACKNOWLEDGMENTS

The authors would like to acknowledge Tim Gilheart, Kung-Po Chao, Sandra Bishnoi, Alex Urban, Jared Day, John Foreman, and Surbhi Lal for productive discussions. This work was supported by the Robert A. Welch Foundation under Grants C-1220 (N.J.H.) and C-1222 (P.N.), the National Security Science and Engineering Faculty Fellowship (NSSEFF) N00244-09-1-0067, the Air Force Office of Scientific Research

(AFOSR) FA9550-10-1-0469, NSF MRI, the Army's in-house laboratory independent research program, and the Army Research Office.

## REFERENCES

- (1) Lal, S.; Link, S.; Halas, N. J. *Nat. Photonics* **2007**, *1*, 641–648.
- (2) Atwater, H. A.; Polman, A. *Nat. Mater.* **2010**, *9*, 205–213.
- (3) Knight, M. W.; Sobhani, H.; Nordlander, P.; Halas, N. J. *Science* **2011**, *332*, 702–704.
- (4) USGS Commodity Statistics and Information. <http://minerals.usgs.gov/minerals/pubs/commodity/> (accessed May 27, 2011).
- (5) Langhammer, C.; Schwind, M.; Kasemo, B.; Zoric, I. *Nano Lett.* **2008**, *8*, 1461–1471.
- (6) Stockli, T.; Bonard, J. M.; Stadelmann, P. A.; Chatelain, A. Z. *Phys. D* **1997**, *40*, 425–428.
- (7) Blaber, M. G.; Arnold, M. D.; Harris, N.; Ford, M. J.; Cortie, M. B. *Physica B* **2007**, *394*, 184–187.
- (8) Andersson, T.; Zhang, C. F.; Tchapyguine, M.; Svensson, S.; Martensson, N.; Bjorneholm, O. *J. Chem. Phys.* **2012**, *136*, 204504.
- (9) Chan, G. H.; Zhao, J.; Schatz, G. C.; Van Duyne, R. P. *J. Phys. Chem. C* **2008**, *112*, 13958–13963.
- (10) Taguchi, A.; Saito, Y.; Watanabe, K.; Yijian, S.; Kawata, S. *Appl. Phys. Lett.* **2012**, *101*, 081110.
- (11) Jha, S. K.; Ahmed, Z.; Agio, M.; Ekinci, Y.; Löffler, J. F. *J. Am. Chem. Soc.* **2012**, *134*, 1966–1969.
- (12) Zoric, I.; Zach, M.; Kasemo, B.; Langhammer, C. *ACS Nano* **2011**, *5*, 2535–2546.
- (13) Ekinci, Y.; Solak, H. H.; Löffler, J. F. *J. Appl. Phys.* **2008**, *104*, 083107.
- (14) Castro-Lopez, M.; Brinks, D.; Sapienza, R.; van Hulst, N. F. *Nano Lett.* **2011**, *11*, 4674–4678.
- (15) Mattiucci, N.; D'Aguanno, G.; Everitt, H. O.; Foreman, J. V.; Callahan, J. M.; Buncick, M. C.; Bloemer, M. J. *Opt. Express* **2012**, *20*, 1868–1877.
- (16) Chowdhury, M. H.; Ray, K.; Gray, S. K.; Pond, J.; Lakowicz, J. R. *Anal. Chem.* **2009**, *81*, 1397–1403.
- (17) Villesen, T. F.; Uhrenfeldt, C.; Johansen, B.; Hansen, J. L.; Ulriksen, H. U.; Larsen, A. N. *Nanotechnology* **2012**, *23*, 085202.
- (18) de Abajo, F. J. G. *Rev. Mod. Phys.* **2010**, *82*, 209–275.
- (19) Kuttge, M.; Vesseur, E. J. R.; Koenderink, A. F.; Lezec, H. J.; Atwater, H. A.; Garcia de Abajo, F. J.; Polman, A. *Phys. Rev. B* **2009**, *79*, 113405.
- (20) Karaveli, S.; Zia, R. *Phys. Rev. Lett.* **2011**, *106*, 193004.
- (21) Vesseur, E. J. R.; de Waele, R.; Kuttge, M.; Polman, A. *Nano Lett.* **2007**, *7*, 2843–2846.
- (22) Gomez-Medina, R.; Yamamoto, N.; Nakano, M.; Abajo, F. J. G. *New J. Phys.* **2008**, *10*, 105009.
- (23) Lassiter, J. B.; Sobhani, H.; Knight, M. W.; Mielczarek, W. S.; Nordlander, P.; Halas, N. J. *Nano Lett.* **2012**, *12*, 1058–1062.
- (24) Chaturvedi, P.; Hsu, K. H.; Kumar, A.; Fung, K. H.; Mabon, J. C.; Fang, N. X. *ACS Nano* **2009**, *3*, 2965–2974.
- (25) Zamoryanskaya, M. V.; Sokolov, V. I. *Semiconductors* **2007**, *41*, 462–468.
- (26) Habteyes, T. G.; Dhuey, S.; Wood, E.; Gargas, D.; Cabrini, S.; Schuck, P. J.; Alivisatos, A. P.; Leone, S. R. *ACS Nano* **2012**, *6*, 5702–5709.
- (27) Palik, E. D. *Handbook of Optical Constants*; Academic Press: San Diego, CA, 1998.
- (28) Papavassiliou, G. C. *Prog. Solid State Chem.* **1979**, *12*, 185–271.
- (29) Gans, R. *Ann. Phys.* **1915**, *352*, 270–284.